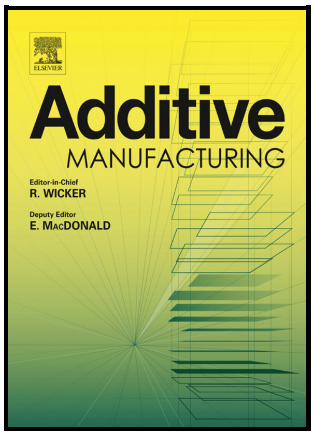

Operando X-ray diffraction study of thermal and phase evolution during laser powder bed fusion of Al-Sc-Zr elemental powder blends

Jennifer A. Glerum, Samy Hocine, Cynthia Sin Ting Chang, Christoph Kenel, Steven Van Petegem, Nicola Casati, Dario Ferreira Sanchez, Helena Van Swygenhoven, David C. Dunand

PII: S2214-8604(22)00207-X

DOI: https://doi.org/10.1016/j.addma.2022.102806

Reference: ADDMA102806

To appear in: *Additive Manufacturing*

Received date: 10 November 2021
Revised date: 3 March 2022
Accepted date: 1 April 2022

Please cite this article as: Jennifer A. Glerum, Samy Hocine, Cynthia Sin Ting Chang, Christoph Kenel, Steven Van Petegem, Nicola Casati, Dario Ferreira Sanchez, Helena Van Swygenhoven and David C. Dunand, Operando X-ray diffraction study of thermal and phase evolution during laser powder bed fusion of Al-Sc-Zr elemental powder blends, *Additive Manufacturing,* (2021) doi:https://doi.org/10.1016/j.addma.2022.102806

Operando X-ray diffraction study of thermal and phase evolution during laser powder bed fusion of Al-Sc-Zr elemental powder blends

Jennifer A. Glerum[a], Samy Hocine[b,c,1], Cynthia Sin Ting Chang[b], Christoph Kenel[a], Steven Van Petegem[b], Nicola Casati[d], Dario Ferreira Sanchez[e], Helena Van Swygenhoven[b,c], David C. Dunand[a]*

[a]*Department of Materials Science and Engineering, Northwestern University, Evanston, IL, USA*
[b]*Photons for Engineering and Manufacturing, Paul Scherrer Institut, Villigen PSI, Switzerland*
[c]*Neutrons and X-rays for Mechanics of Materials, IMX, École Polytechnique Fédérale de Lausanne, Switzerland*
[d]*Materials Science Beamline, Paul Scherrer Institut, Villigen PSI, Switzerland*
[e]*MicroXAS Beamline, Paul Scherrer Institut, Villigen PSI, Switzerland*

[1]*Currently: Department of Mechanical Engineering, University College London, London, England*

*Corresponding author: dunand@northwestern.edu

keywords: selective laser melting, operando diffraction, elemental blends, additive manufacturing, aluminum

Abstract

Elemental powder blends are an emerging alternative to prealloyed powders for high-throughput alloy design *via* additive manufacturing techniques. Elemental Al+Sc(+Zr) powder blends were processed by laser powder bed fusion into Al-Sc and Al-Sc-Zr alloys, with *operando* X-ray diffraction at the Swiss Light Source extracting the structural and thermal history of the process. The pure Sc and Zr particles were found to react with the molten Al pool at 550-650 °C, well below their respective melting temperatures. Various scan areas (1×1, 2×2, 4×4, and 8×2 mm^2) were studied to compare (i) the base plate "preheating" effect caused by prior laser scans, (ii) the return temperature reached after the melting scan and before the following scan, (iii) the initial cooling rate immediately after solidification, and (iv) the time spent in the "intrinsic heat treatment range", defined as 300-650 °C, where secondary precipitation occurs. Microstructural analysis of the as-built samples show 110-140 nm $L1_2$-Al_3(Sc,Zr) primary precipitates at the bottom of the melt pool. The 1×1 mm^2 samples exhibit the most elongated grains (long axis of 10 ± 5 μm), which correlates with the highest build plate temperature and the slowest initial cooling rate (3-5 × 10^5 K/s). In comparison, the 4×4 mm^2 samples exhibit the smallest equiaxed grains (2 ± 0.6 μm), corresponding to the lowest build plate temperature and the fastest initial cooling rate (6-7 × 10^5 K/s). These results indicate the need for establishing a minimum feature size during part design or for modifying the laser parameters during processing to mitigate microstructure and performance differences across features of different sizes.

1 Introduction

Laser powder bed fusion (L-PBF) is the most commonly used additive manufacturing (AM) technique for aluminum alloys [1]. Early work has focused on Si-containing cast alloys (AlSi10Mg, AlSi7Mg) due to the easily-achievable high density and low susceptibility to cracking; however, these cast alloys are not suitable for usage at high temperatures (>250 °C). Subsequent L-PBF studies incorporated Zr in Si-free Al alloys, leading to formation of primary $L1_2$-Al_3Zr to nucleate small, equiaxed Al grains with a high resistance to hot cracking [2].

Most powder-bed AM processes use prealloyed powder, in which each powder particle contains all constituent elements in the same ratio as in the final alloy. This technique is cost-efficient for industrial-scale production of parts with optimized compositions, but not for the alloy design process, which may require many iterations of different elements in different ratios. An alternative AM approach uses mixed elemental powders, as demonstrated in directed energy deposition (DED) of high entropy alloys (HEAs) [3-11], and in L-PBF of binary alloys such as Ti-X (X = Ni, Nb, Ta, Al, V, Zr, Cr, Mo) [12-22], Ni-Sn [23], Fe-Cu [24], Al-Cu [25, 26], and Al-Si [27-29]. Prior work showed the dissolution and reaction process during L-PBF single-line scans of elemental blends of Al-Sc, Al-Zr, and Al-Sc-Zr to create compositionally- and microstructurally-homogeneous dilute alloys [30], expanding the ability to design precipitation-strengthened Al-base alloys from elemental blends. The present study builds on that prior work by investigation, *via* synchrotron X-ray diffraction, the *operando* dissolution and reaction of elemental Sc and Zr particles in the Al matrix during layer-wise printing of bulk samples.

In situ and *operando* synchrotron studies of single melt pool tracks, constituent phase evolution, and the entire layer-wise AM process have been performed previously using *in situ* X-ray imaging [31, 32] and diffraction [33, 34] during L-PBF. Melt pool spatter, particle interactions, Marangoni convection and flow, and porosity formation have been the focus of multiple *in situ* synchrotron X-ray imaging studies [35-42]. Hocine et al. built the miniSLM - a custom, portable small-scale L-PBF machine compatible with multiple beamlines at the Swiss Light Source - to directly observe the phase evolution of Ti-6Al-4V in small-scale builds *via* synchrotron X-ray diffraction [43, 44]. In the present work, this instrument is employed for the first time on Al-base alloys.

When progressing from single-line scans to full multilayer AM builds, generating a laser scan path to fill the processing area in an optimal way is an entire area of work within the AM field [45]. The scan path affects not only build time and surface roughness, but also heat accumulation, solidification rate, and resulting microstructure, which affect the properties of the consolidated material. A popular tool path to reduce residual stresses and warpage is a “checkerboard” or “island pattern” strategy[46], subdividing a large area into small fields scanned in a random order. Previous work has reviewed the microstructure, mechanical properties, and residual stresses of the nickel-base alloy INCONEL 718 printed with 2×2, 3×3, 5×5, and 7×7 mm^2 square areas [47]. The present study investigates the effect of different island sizes (1×1, 2×2, 4×4, and 8×2 mm^2) on the microstructure of Al-Sc(-Zr) printed parts, to inform tool-path selection for L-PBF Al alloys in the future.

In this work, the reaction of elemental Sc and Zr powders with liquid aluminum is observed directly *via operando* diffraction in Al-Sc and Al-Sc-Zr powder blends during L-PBF, with a temporal resolution of 50 µs. The Sc/Zr dissolution into the Al melt pool is followed by precipitation of primary $L1_2$-Al_3Sc and -$Al_3(Sc,Zr)$ phases, respectively, which act as grain refiners, thus enabling crack-free AM processing of Al alloys. Excess Sc and Zr remain in supersaturated solid solution in the Al matrix and are available for

secondary precipitation of $L1_2$ nanoprecipitates upon aging heat-treatments. From the *operando* diffraction data, the local thermal history for each sample is extracted *via* the measured lattice expansion, providing quantitative measurements of (i) the influence of scan area size on the heat buildup prior to melting, (ii) the return temperature reached between subsequent laser passes, (iii) the initial cooling rate immediately after solidification, and (iv) the time spent in the intrinsic heat treatment range (300 – 650 °C) after each laser pass, which can cause precipitation of secondary phases over an entire multilayer build.

2 Materials and Methods

2.1 Elemental powder characterization and mixing

Powders of aluminum (99.7% pure, 30 µm average size, from US Research Nanomaterials, Inc.), scandium (99.5% pure, 44 µm average size, from Nanografi Inc.), and zirconium (99% pure, <44 µm size, from US Research Nanomaterials, Inc.) were combined to create Al-Sc and Al-Sc-Zr elemental blends, as shown in Table 1. The powders were mixed by rotational ball-milling for 3 h in an argon atmosphere, using yttria-stabilized zirconia balls (6.5 and 12 mm diameter) in high-density polyethylene vials at a 5:1 ball-to-powder ratio. This low-energy blending does not mechanically alloy the powders, which maintain a round shape for good flowability. More details can be found in a previous study [30]. The elemental powders were examined *via* SEM and energy dispersive X-ray spectroscopy (EDS) to determine their morphology, as shown in **Figure 1.**

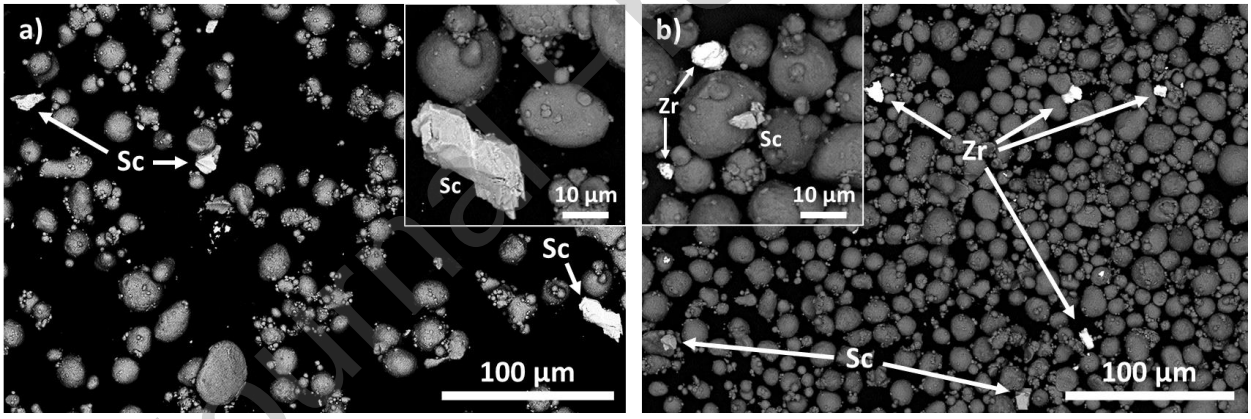

Figure 1: SEM micrographs of powder blends of binary Al-Sc **(a)** and ternary Al-Sc-Zr **(b)**, showing Sc (light grey) and Zr (white) powder distributed among Al powders after low-energy ball milling; insets show higher magnification of the rounded Al particles with small Al satellites and angular, faceted Sc and Zr particles.

Table 1. Compositions of Al-Sc(-Zr) elemental powder blends used for L-PBF.

Alloy	Sc	Zr
Al-Sc	0.52 at.% 0.86 wt.%	-
Al-Sc-Zr	0.26 at.% 0.43 wt.%	0.26 at.% 0.87 wt.%

2.2 Laser powder bed fusion via *miniSLM*

Offline manufacturing of the different alloys was performed to establish a set of optimized laser parameters maximizing the build density prior to the *operando, in situ* experiments. The experimental setup enlisted the miniSLM, a custom-built, small-scale L-PBF machine; details are given in previous works by Hocine et al. [43, 44]. In brief, the miniSLM is a self-contained chamber which can be mounted in a beamline and tilted up to 20° for *operando* X-ray experiments in either transmission or reflection mode. The chamber, containing a 12 × 12 mm^2 build plate with a 10 × 10 × 5 mm^3 available build volume, is continuously flushed with high-purity Ar (99.998%) gas during printing and is equipped with a high-energy, continuous-wave laser beam with a 1070 ± 10 nm wavelength and a maximum power of 500W, mounted on a 2-axis scanning unit. For this work, a constant laser spot size of 100 µm was used. The baseplates for L-PBF were machined from a rod of 99.999% pure Al (Goodfellow, Inc.) instead of other commonly used alloys (e.g., AlSi10Mg) to minimize contamination from the baseplate into the elemental powder blends. Processing was performed with a variety of laser parameter combinations, ranging from 200 to 400 W power, 200 to 675 mm/s beam velocity, 30 to 70 µm layer thickness, and 70 to 90 µm hatch spacing, corresponding to energy densities between 90 and 312 J/mm^3 where energy density is given as $\Psi = P/(v * h * t)$ (P = power in W, v = velocity in mm/s, h = hatch spacing in mm, and t = layer thickness in mm). Previous *in situ* X-ray imaging experiments using comparable laser parameters (P = 350 W, v = 350-600 mm/s) resulted in conduction mode, which is taken to be the case in this work [30]. Ten sets of laser parameters producing the densest builds were selected from this range, with energy densities of 225 and 259 J/mm^3, as shown in Table 2.

Table 2. Laser parameter combinations for L-PBF of Al-Sc and Al-Sc-Zr.

Laser power (W)	Scan speed (mm/s)	Hatch spacing (µm)	Layer thickness (µm)	Energy density (J/mm^3)
325	451	80	40	225
325	392	80	40	259
350	389	80	50	225
350	338	80	50	259
350	486	80	40	225
350	423	80	40	259
375	417	80	50	225
375	362	80	50	259
375	521	80	40	225
375	452	80	40	259

2.3 Operando *X-ray diffraction*

Operando X-ray diffraction was performed in reflection mode at the Swiss Light Source (SLS) at the Materials Science beamline (MS-X04SA), using a monochromatic 12 keV beam on an 8×2 mm^2 rectangular laser scan area (**Figure 2**, top), and at the microXAS beamline (X05LA) using a monochromatic 9.3 keV beam in a series of 1×1, 2×2, and 4×4 mm^2 laser scan areas (**Figure 2**, bottom). Multiple layers (at least five per sample) were built for each sample geometry, with several-minute-long pauses between subsequent layers for static diffraction patterns to be recorded.

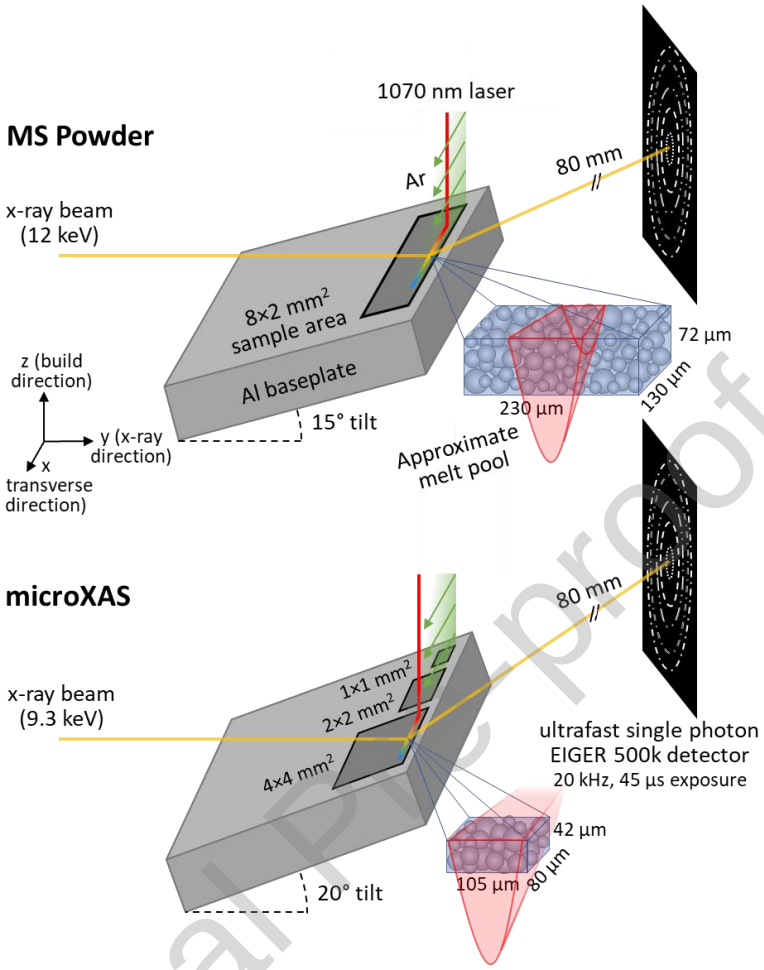

Figure 2: Schematic of build geometry at the MS beamline (top) and at the microXAS beamline (bottom), showing approximate diffraction volume (shown in blue) and melt pool volume (shown in red), with powder to scale. The Ar shielding gas is shown in green, entering from left to right across the sample as viewed from the beam source.

An 8×2 mm^2 sample area was printed at the MS beamline, and 1×1, 2×2, and 4×4 mm^2 square sample areas were printed at the microXAS beamline, with a bidirectional scan strategy and 90° layer rotation. The diffraction volume was focused at the horizontal center of each sample area during laser scanning and at the downstream end of the scan area (as illustrated in **Figure 2**). The sample was positioned 80 mm from an ultrafast single photon EIGER detector, shown on the right side of the schematic in **Figure 2**.

The X-ray beam at the MS beamline was focused to 130$\hat{x}$ × 60$\hat{y}$ µm^2 (FWHM) and the sample was tilted at a 15° angle with respect to the X-ray source, resulting in a projected area of 130$\hat{x}$ × 230$\hat{y}$ µm^2 and allowing an X-ray penetration depth of 72$\hat{z}$ µm into the sample, estimated assuming 10% transmission through the sample. The X-ray beam at the microXAS beamline was focused with Kirkpatrick-Baez mirrors to 80$\hat{x}$ × 36$\hat{y}$ µm^2 (FWHM) and the sample was tilted at a 20° angle with respect to the X-ray source, resulting in a projected area of 80$\hat{x}$ × 105$\hat{y}$ µm^2 and allowing an X-ray penetration depth of 42$\hat{z}$ µm into the sample, estimated in the same way. The tails of the beams extend to roughly twice the projected areas; thus, the majority (~63%) of the signal originates from particles located in the FWHM of

the beam, but some signal from particles located in the tails of the beams may be captured as well. **Figure 2** shows the approximate diffraction volumes (using the FWHM) of the experimental setups at the MS (top) and microXAS (bottom) beamlines, with 15-30 µm powder particles included within each diffraction volume for scale. Depending on the specific particle size distribution, approximately 50-100 particles are contained within a given MS diffraction volume and 10-20 within a given microXAS diffraction volume. The atomic compositions of Al-0.52Sc and Al-0.26Sc-0.26Zr (at.%) are equivalent to volumetric compositions of Al-0.78Sc and Al-0.39Sc-0.37Zr (vol.%); assuming all Al, Sc, and Zr particles are approximately the same size, this equates to one Sc or Zr particle for every 130 Al particles. Thus, the diffraction volume at the MS beamline has a much higher probability of capturing a Sc or a Zr particle during the *operando* experiment than the diffraction volume at the microXAS beamline. Conversely, the smaller beam at the microXAS beamline provides less volume-averaging for temperature measurements. An approximate melt pool is overlaid in red on the two diffraction volumes represented in blue in **Figure 2**, illustrating how the melt pool is not expected to melt the entirety of the MS diffraction volume, but is expected to melt all the microXAS diffraction volume. Further details are given in previous works by Hocine et al. [43, 44].

The diffracted beam is captured by an in-house-developed ultrafast EIGER 500k detector positioned at a distance of ~80 mm from the sample along the X-ray beam direction ($\hat{y}$), at a frame frequency of 20 kHz, and an exposure time of 45 µs [48]. The setup was calibrated with the diffraction signal of quartz powder, yielding the sample-to-detector distance, beam center and detector tilt. This single-photon-counting hybrid detector, with an area of ~8×4 cm^2, contains 500,000 pixels with a pixel size of 75×75 μm^2, and it can store 30,000 recorded patterns in 4-bit mode. During the *operando* measurements, up to 20,000 2D diffraction patterns were acquired for each printed layer. These 2D patterns were azimuthally integrated and reduced to 1D diffraction patterns via the Bubble software package [49], which is based on pyFAI, a Python library for fast integration [50]. A MATLAB script developed in-house was used to calculate the center of mass of selected Al/Sc/Zr peaks and track their locations and intensities over time; these peak locations were then used to extract the temperature shifts using the respective planes' coefficients of thermal expansion.

2.4 Microstructure characterization

The top surface of selected samples deposited during beamline experiments were lightly polished to a 0.04 µm finish with a standard fumed-silica suspension from Struers to remove top surface texture and reveal bulk porosity and composition. The samples were then cut perpendicular to the surface and the cross-sections were polished to a 0.02 µm finish with a non-crystallizing colloidal silica suspension. A Leica TIC3X triple ion beam miller was used at 6.0 kV and 2.2 mA, with a flat milling stage angled at 6°. Both top and cross-sectional areas were examined with a FEI Quanta 650 scanning electron microscope (SEM) with secondary electron (SE), backscatter electron (BSE), and energy dispersive X-ray spectroscopy (EDS) detectors, and a JEOL JSM-7900-FLV SEM with SE, high-sensitivity BSE, and EDS detectors. Particle size analysis was performed using ImageJ.

3 Results and Discussion

3.1 Operando *reaction of Sc and Zr with Al*

High-speed *operando* diffraction to study the reaction of Zr and Sc was performed at the MS powder beamline featuring a larger diffraction volume during the L-PBF of elemental powder blends with target composition of Al-0.52Sc and Al-0.26Sc-0.26Zr. The larger diffraction volume of ~130 × 230 × 72 μm^3 increases the probability to observe a Zr or Sc particle within the blend at a ratio of ~1:130 by volume. **Figure 3** shows the phase and temperature evolution in **(a-c)** Al-Sc and **(d)** Al-Sc-Zr, during laser scanning of 8×2 mm^2 blocks. **Figure 3a** shows the evolution of diffraction patterns for an Al-Sc sample (power: 375 W, scan speed: 521 mm/s, hatch spacing: 80 µm) from t = 0 to 700 ms, where t = 0 corresponds to the start of printing; however, the laser is far from the diffraction volume, and so t = 0 shows diffraction data collected from the Al-Sc(-Zr) powder blend layer prior to laser interaction. The data are shown as logarithmically color-mapped diffraction intensity as function of time (on the y-axis) and diffraction angle (on the x-axis). Due to a low number density of Sc and Zr powders within the diffraction volume, combined with random crystal orientation, Sc/Zr single peaks are observed only in a fraction of the experiments. Here, the (0002) diffraction of a favorably-oriented Sc particle is observed in the powder bed and persists to 316 ms, where it abruptly disappears. **Figure 3b** shows a reduced angle and timescale view of the diffraction data in **Figure 3a**. While the X-ray beam, and thus the observation point, is centered and fixed in the long dimension of the 8×2 mm^2 rectangular scan area, the laser is scanning over the full area with a hatch spacing of 80 µm. At the fixed observation location, the laser passes by in close proximity multiple times, leading to thermal expansion of the Al powders in the diffraction volume, observed as a shift towards a smaller diffraction angle. This sharp peak shift is followed by a gradual return to the centerline upon cooling, before the next laser pass causes the expansion/contraction cycle to repeat. Due to the size of the diffraction volume (130 × 230 μm^2) compared to the hatch spacing (80 µm), combined with the high thermal conductivity of Al, thermal lattice expansion is observed prior to the laser passing directly through the observed volume. From a processing perspective, this leads to a preheating of the powder bed prior to the melt scan.

After the melting event, the subsequent laser scan vectors re-heat the solidified diffraction volume on each pass until the passes are sufficiently far away. This leads to a complex thermal history within a single solidified layer, with a series of rapid thermal-cycling treatments of diminishing intensity. In these experiments, the diffraction volume (~130 × 230 × 72 μm^3) is larger than the melt pool size, and thus solid material from the melt pool edges is always observed in diffraction, consistent with the diffraction pattern never disappearing completely (as would be expected if all the material within the diffraction volume were molten at the same time). The pattern repeat time is defined as the time the laser reaches the end of the scan area, turns around and again reaches the location of the X-ray beam; i.e., when scanning the 8×2 mm^2 area, the laser travels 4 mm to the edge, turns around and travels another 4 mm within ~16 ms to reach the observation location again.

Figures 3c and **d** shows the estimated average temperature of the phases within the diffraction volume, calculated from the peak shifts during laser scanning. The (111), (200), and (220) peaks of the face-centered cubic α-Al phase were tracked from before to after the laser melting event, as were the (0002) peak of hexagonal close-packed (h.c.p.) pure Sc observed in an Al-Sc sample and the $(11\bar{2}0)$ peak of h.c.p. pure Zr in an Al-Sc-Zr sample. Based on known thermal lattice expansion of the pure Al (27×10^{-6} K^{-1}), Sc (15×10^{-6} K^{-1}), and Zr phases (11×10^{-6} K^{-1}) [51, 52], the temperature can be calculated from the measured change in lattice parameter during the heating events. Various sources of errors exist. First, the lattice expansion is assumed to be solely due to thermal expansion from heating, not accounting for the effect of residual stresses or compositional changes. If tensile stresses arise, the estimated

temperatures are an upper bound and may overestimate the actual temperatures experienced by the samples; if compressive stresses arise, the calculated temperature is underestimated. Second, the conversion from lattice expansion to temperature of the Al peaks was performed assuming a constant coefficient of thermal expansion (CTE) of 26.7×10^{-6} K^{-1}, which is an average value corresponding to the CTE around 280 °C. In reality, the CTE is temperature-dependent, and this analysis using constant CTE leads to a ~5% overestimation of the temperatures experienced by the melt pool, compared to the analysis performed with variable CTE vs. temperature. However, this simplification was determined not to change the results given in **Figures 3-5**. A full comparison of the analyses using constant vs. variable CTE is given in the Supplemental Information (**Figures S1-S4)**. Third, the diffraction volume extends into colder regions, leading to an averaging of lattice parameter across a temperature gradient within the Al matrix. Temperatures for the Al matrix determined by *operando* X-ray diffraction are thus a volume average. In contrast, the temperatures determined for single Sc and Zr particles captured in the diffraction volume are only averaged over the particle volume (~30 µm diameter), the only place where pure Zr/Sc exists. These single particles can thus be used as temperature probes with higher spatial resolution compared to the surrounding Al matrix.

In **Figures 3c** and **d**, the Sc(0002) and Zr($11\bar{2}0$) peaks become too weak to detect at times t=316 and 400 ms, respectively. Based on the observed maximum temperatures of 350 and 405 °C, respectively, the Sc and Zr particles tracked here are assumed to have reacted with the Al melt and not have been ejected from the melt pool, in which case no temperature increase would be observed due to the fixed location and size of the X-ray beam. For comparison, an example of an Sc/Zr particle ejected from the melt area prior to melting can be found in the Supplemental Information (**Figure S5**). The maximum calculated temperatures from the Sc and Zr peaks in **Figures 3(c,d)** are close to the temperature observed in the Al matrix, indicating that the particles react with the Al melt at a temperature (400-650 °C) close to the melting point of Al (662 °C), rather than being directly heated to the melting point of Sc or Zr (1541 and 1855 °C, respectively) by the laser. This is in agreement with prior work, where reaction of solid Sc and Zr particles with molten Al was observed during *in situ* high-speed imaging experiments of a single laser scanning line [30].

In **Figure 3d,** the temperatures in the solidified diffraction volume, calculated from the Al (111), (200), and (220) peaks, differ by up to ~100 °C at 700 ms. The Al(111) direction yields the highest temperature, while the Al(200) direction shows the least lattice expansion and thus lowest calculated temperature. Physically, the crystals' diffraction should be very close in temperature. The difference between the directions is thus likely caused by internal stresses arising during solidification and cooling. Based on the diffraction geometry of a 15° tilt of the miniSLM chamber and the diffraction angle of ~28°, the observed (200) direction is closest to the surface normal (30°) of the specimen, in comparison to the (111) and (220) directions with diffraction angles of ~24° and ~40°, respectively. As such, the observed (200) planes are least affected by the large horizontal tensile stresses that typically arise during L-PBF [53]. Thus, the Al(200) direction provides the most consistent temperature estimation across different experiments.

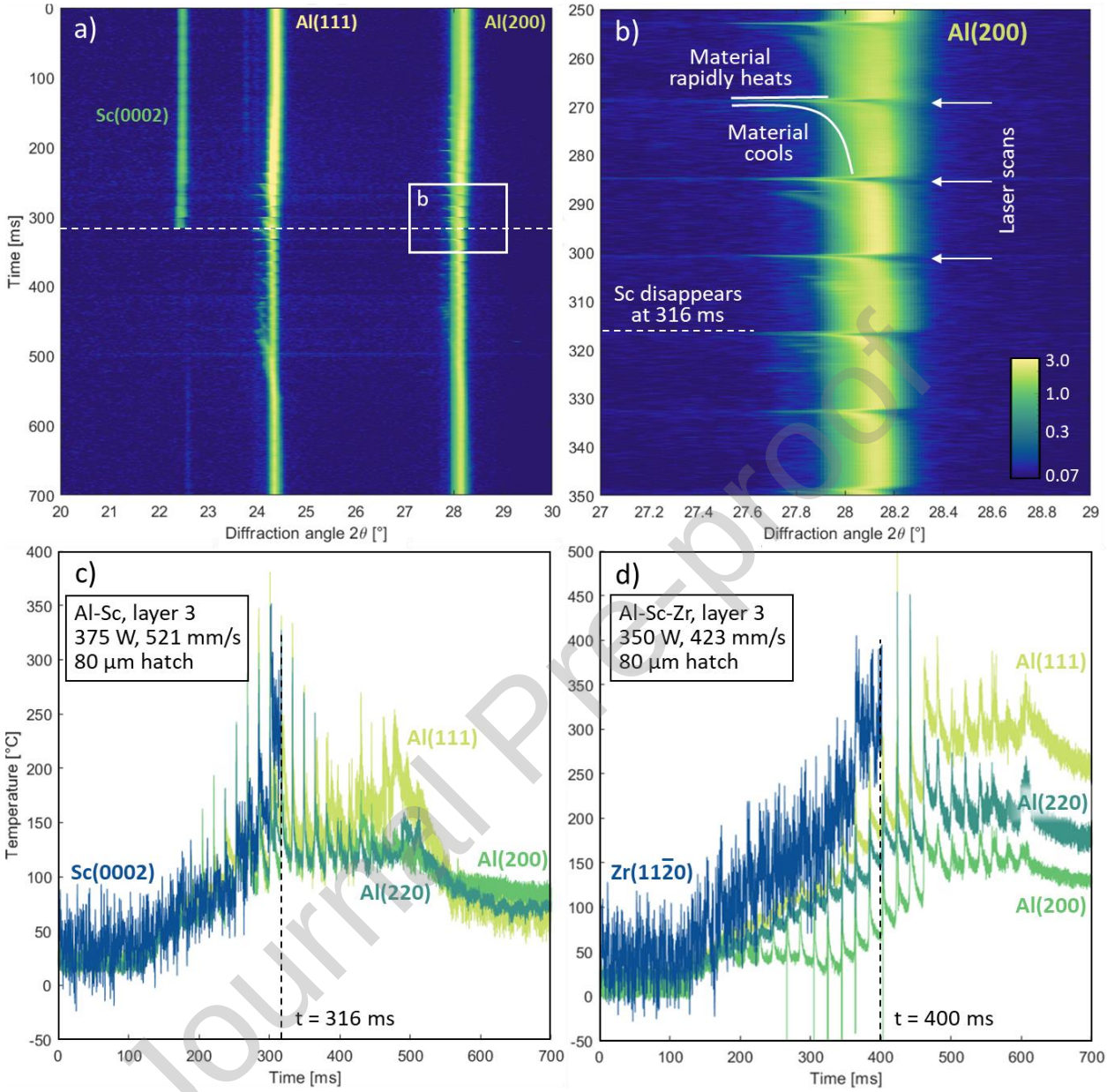

Figure 3: Diffraction patterns and calculated thermal profile of Al-Sc and Al-Sc-Zr alloys during *operando* L-PBF at the Materials Science beamline of the SLS. **(a)** Evolution of the diffraction patterns vs. time for Al-0.52Sc, showing the Al(111) and Al(200) peaks before and after the melting of Sc (at 316 ms, visible from the disappearance of the Sc(0002) peak). **(b)** Reduced timescale and angle view of white box in **(a)**, showing the shape of each heating/cooling cycle for the Al(200) peak, ~16 ms apart. Intensity (counts per pixel) is color-mapped on a log scale, where the baseline is shown in dark blue and peaks rising above the baseline are shown in green/yellow. **(c)** Evolution of temperature in an Al-0.52Sc sample, as calculated by the peak shifts and thermal expansion coefficients of the Al(111), Al(200), Al(220), and Sc(0002) peaks. The Sc particle shows an increase in temperature to 350 °C until it disappears at t = 316 ms, indicating its reaction in the Al melt. **(d)** evolution of temperature in an Al-0.26Sc-0.26Zr sample as calculated using the Al(111), Al(200), Al(220), and Zr(11$\bar{2}$0) peaks. The temperature of the Zr particle increases to 405 °C until it disappears due to reaction with the Al melt at t = 400 ms.

Figure 4 shows the evolution of the elemental Sc **(a-b)** and Zr **(c)** peak intensities in counts per pixel decreasing over six timesteps of 50 µs intervals (300 µs total) as the laser interacts with the diffraction volume containing elemental Sc/Zr particles. **Figures 4(a-b)** and **4c** correspond to the experiments described in **Figures 3c** and **3d**, respectively; **Figure 4b** likely captures a different grain within the same Sc particle as in **Figure 4b**, as the timing of the reaction is identical in both. This time scale lines up with previously observed interactions between Sc/Zr elemental particles with molten Al droplets [30].

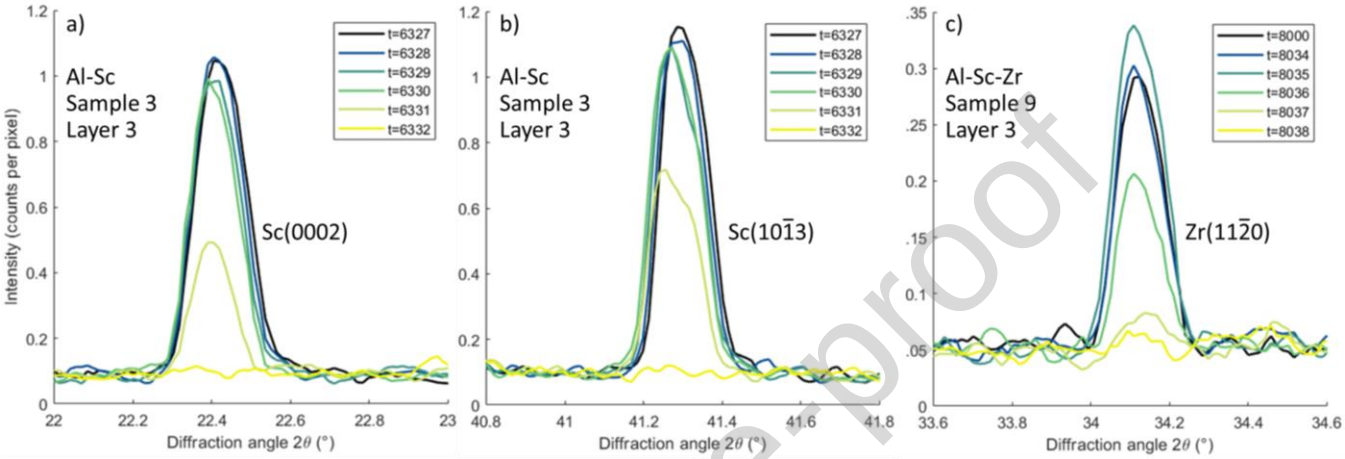

Figure 4: Progression of **(a)** Sc(0002) peak, **(b)** Sc(10$\bar{1}$3) peak, and **(c)** Zr(11$\bar{2}$0) peak from before (black) to after (yellow) laser interactions, captured over 6 timesteps, 50 µs apart (300 µs total).

3.2 Influence of scan area size on thermal history

High-speed *operando* X-ray diffraction to study the influence of the scan area size on the temperature history of the alloys is performed at the microXAS beamline on the same Al-Sc and Al-Sc-Zr elemental powder blends with a diffraction volume of ~80×105×42 µm. **Figure 5** shows four representative temperature evolution curves from the 1×1 (yellow), 2×2 (green), and 4×4 (teal) mm^2 samples of an Al-Sc powder layer processed with laser parameters of 375 W, 521 mm/s, 80 µm hatch spacing, and 40 µm layer thickness, which corresponds to a volumetric energy density of 225 J/mm^3. Additionally, the data from the MS powder beamline featuring an 8×2 (blue) mm^2 scan area are shown for comparison. Depending on the layer number, the 8×2 mm^2 field was scanned along its short or long direction, yielding additional information for scan vector lengths of 2 and 8 mm. The Rosenthal equation [54] - an analytical solution for the three-dimensional heat distribution for a moving heat source - was used as an approximation to fit the shape of the thermal profiles:

$$T(x,R) = T_0 + \frac{Q}{2\pi R k_T} * \exp\left(-\frac{v}{2\alpha}(R+x)\right) \quad (1a)$$

where $R = \sqrt{x^2+y^2+z^2}$ and where T_0 is the original temperature of the powder bed upon laser scanning, k_T is the thermal conductivity, $\alpha = \frac{k}{c_p \rho}$ is the thermal diffusivity (where k is the thermal conductivity in W/mK, c_p is the specific heat capacity in J/(kg*K), and ρ is the density in kg/m^3), v is the laser scan speed, and Q is the absorbed power.

The Rosenthal equation can be simplified to:

$$T(x,R) = T_0 + \frac{Q}{2\pi k_T} * \frac{1}{-x} \quad (1b)$$

by choosing R, the location of interest, to be -*x*, which is the farthest point on the surface of the trailing edge of the melt pool. The spatial coordinate *x* can then be related to time with $x_{rel} = x - x_0 - v * t = \bar{x} - v * t$, where x is the real x-coordinate in space, x_0 is the location of the laser at t_0, and x_{rel} describes the constant x-coordinate relative to the laser through time t. An x-coordinate of 150 µm was selected as an approximation for the tail end of the surface melt pool. The Rosenthal equation can then be expressed in the form:

$$T(t) = \frac{a}{(t-c)} + b, \quad (1c)$$

where a, b, and c are constants. Fitted thermal profiles based on the Rosenthal equation are shown overlaid in black in **Figure 5**.

The size of the scanned field (i.e., the length of the scan vector) affects the preheating temperature before melting, the duration of the preheating, the return temperature after melting until the next laser pass starts, and the time between individual laser passes. With increasing field area, the preheating time is increased, as it takes more time for the laser to travel the longer distance. As heat flow is limited by thermal conductivity, a smaller scanned field experiences a higher preheating temperature as the laser returns within a shorter period of time, adding more energy into the material. With a higher baseline temperature achieved by preheating, the temperature after the melting scan (defined here as the scan reaching the highest observed temperature in the crystalline Al matrix surrounding the melt pool) is also increased with smaller scan sizes. The combination of these effects can be considered as a base plate "preheating" effect, which is dependent on scan area size. Additionally, the scan repeat time between consecutive heating/cooling cycles is marked in **Figure 5** for all four curves. The high temporal resolution of the X-ray diffraction experiment allows to determine a 0.4-0.6 ms delay in beam optics when turning the laser beam around, which matches well with a calculated settling time of 0.63 ms from previous experiments [55]; this is the difference between the calculated scan repeat times (1.9, 3.8, 7.7, and 15.4 ms, based on the scan speed of 521 mm/s) and the measured repeat times (2.3, 4.4, 8.2, and 16.1 ms).

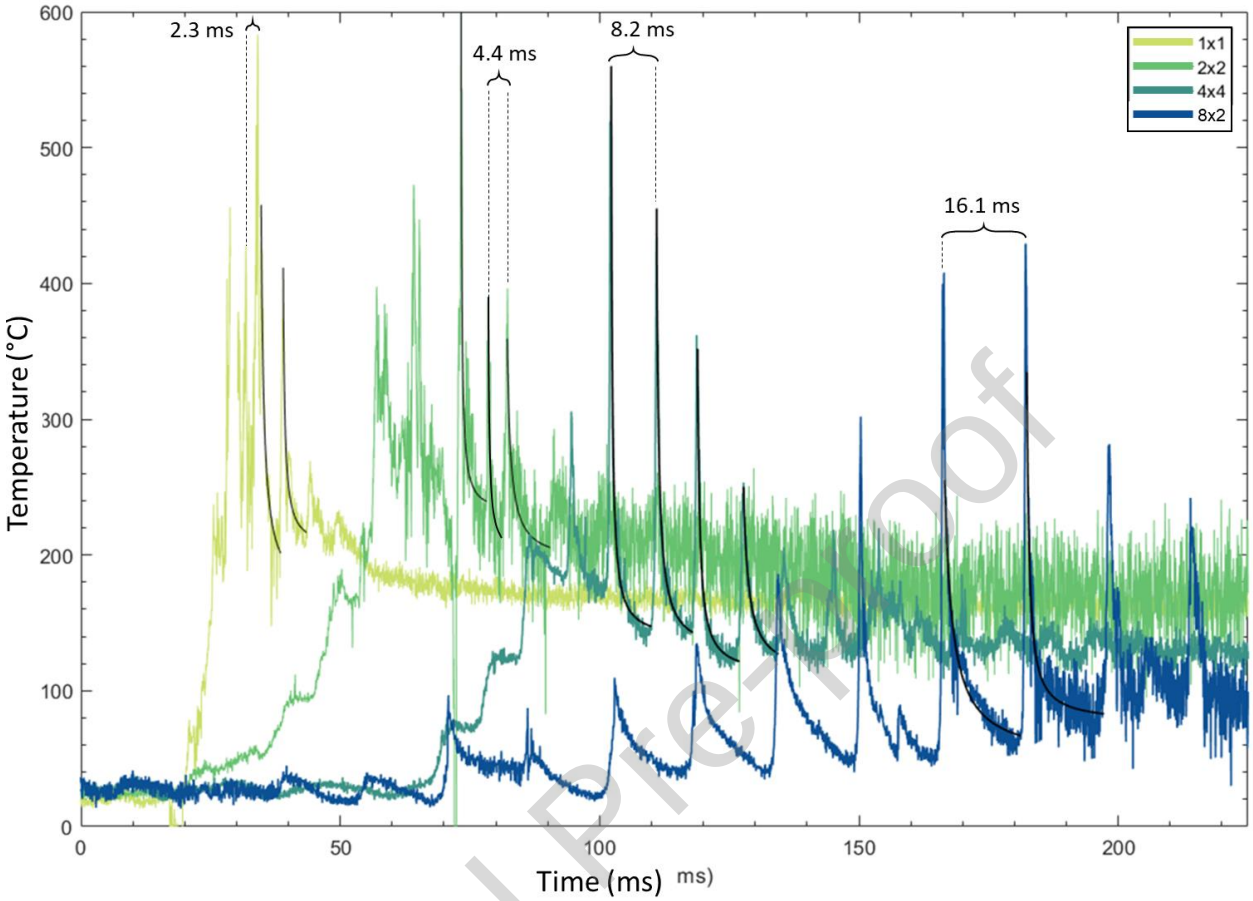

Figure 5: Influence of scan area on local heat accumulation. Temperature evolution, calculated from Al (200) lattice expansion of the 1×1 mm^2 (yellow), 2×2 mm^2 (green), 4×4 mm^2 (teal), and 8×2 mm^2 (blue, in the 8 mm scan direction) fields for Al-0.52Sc samples, printed at 375 W, 521 mm/s, 80 µm hatch spacing, and 40 µm layer thickness (volumetric energy density of 225 J/mm^3). Fits using the Rosenthal equation are overlaid in black, which provide information on time between laser passes and on the return temperature achieved between consecutive laser passes.

Figures 6(a-d) show **(a)** an example temperature profile of Al-0.52Sc processed at 375 W and 417 mm/s, and **(b-d)** three parameters, extracted and averaged over all *operando* experiments, as a function of scan vector length and alloy type, namely: **(b)** the return temperature between the melt scan and the subsequent scan, **(c)** the initial cooling rate in the solid Al after the melt scan, and **(d)** the time spent in the intrinsic heat treatment range (300-650 °C) after the melting event. The three square field samples (1×1, 2×2, and 4×4 mm^2) were measured at the microXAS beamline. The 8×2 mm^2 samples were measured at the MS beamline: alternating layers (in the long and short directions) were used to collect data for the 8- and 2-mm scan vectors respectively, allowing comparison with the square field data. The return temperature and initial cooling rate are calculated from only a single curve per layer, which experienced the highest temperature and steepest initial cooling rate, defined as the "melt scan"; by contrast, the time spent in the intrinsic heat treatment range is a sum of all times spent between 300-650 °C after the full melting curve. The return temperature is estimated by fitting the selected curve to the form of the Rosenthal equation (Eq. 1(c)), where *b* is the y-asymptote as time approaches infinity. The return temperature is then defined as the last temperature prior to the temperature increase of the

subsequent scan (**Figure 6a**). The initial cooling rate is estimated by fitting the highest-temperature data with a linear approximation, which is validated by the analysis performed on similar data with Ti-6Al-4V on the same experimental setup [55]. The time spent in the intrinsic heat treatment range is calculated using the linear fit between 300 and 650 °C.

For the scan sizes studied here, the observed return temperature decreases with increasing scan vector length (**Figure 6b**), indicating that the larger samples reach a lower temperature before the subsequent laser scan, as expected. The average temperatures in a 1×1 mm^2 field reach ~200 °C, but they drop to ~100 °C in scans which are 4 mm and longer.

The samples also show an increase in cooling rate with the increasing scan vector size (**Figure 6c**); the 1×1 mm^2 sample experienced the lowest cooling rate of 3-5 × 10^5 K/s, compared to 5-6 × 10^5 K/s for the 2×2 mm^2 sample, and 6-7 × 10^5 K/s for the 4×4 mm^2 and 8×2 mm^2 samples. With an increased scan vector length, the lower temperature within the surrounding area leads to a larger temperature gradient, as more time passes between consecutive laser scans and thus more heat is removed into the baseplate by thermal conduction. This difference in thermal gradient and solidification rates is expected to affect the resulting microstructure: changing solidification speed in the melt pool leads to the nucleation of more $L1_2$-Al_3(Sc,Zr) precipitates, which in turn nucleate smaller, equiaxed α-Al grains. Conversely, a constant solidification speed traps Sc/Zr solute in the melt and nucleates fewer $L1_2$-Al_3(Sc,Zr) precipitates, leading to fewer, more elongated grains. These results are further discussed in Section 3.3.

The time spent by the samples in the intrinsic heat-treatment region can be estimated using the linear fits up to 650 °C, the temperature at which the material is expected to solidify, and down to 300 °C, the temperature below which Sc and Zr diffusion in Al becomes slow. In this temperature range, precipitation of secondary phases is possible. The approximate times spent within this intrinsic heat treatment regime for each laser pass are shown in **Figure 6d**. The recently solidified material in the 1×1 and 2×2 mm^2 samples spend the longest time (1.0-1.3 ms) above 300 °C, compared to 0.7-0.9 ms for the 4×4 and 8×2 mm^2 samples. Although 1 ms is far too short to precipitate any nanoscale secondary phases in a single laser pass, the cumulative effects of this varying intrinsic heat treatment could become significant in a larger, multilayer build with different feature sizes. Layer-wise AM reheats the underlying material, so in a full build, the material experiences numerous such intrinsic heat treatment cycles. If sufficient time and temperature is provided, precipitation of secondary $L1_2$ or other phases may occur by the end of the build, depending on the precipitation kinetics of the alloy.

In summary, the observed return temperature, cooling rate, and intrinsic heat treatment time all approach a constant value for scan vector lengths greater than 4 mm. Any island-scan strategy using shorter scan vectors, or any feature with a smaller cross-section, will experience a higher cooling rate and return temperature and spend more time in the intrinsic heat treatment regime.

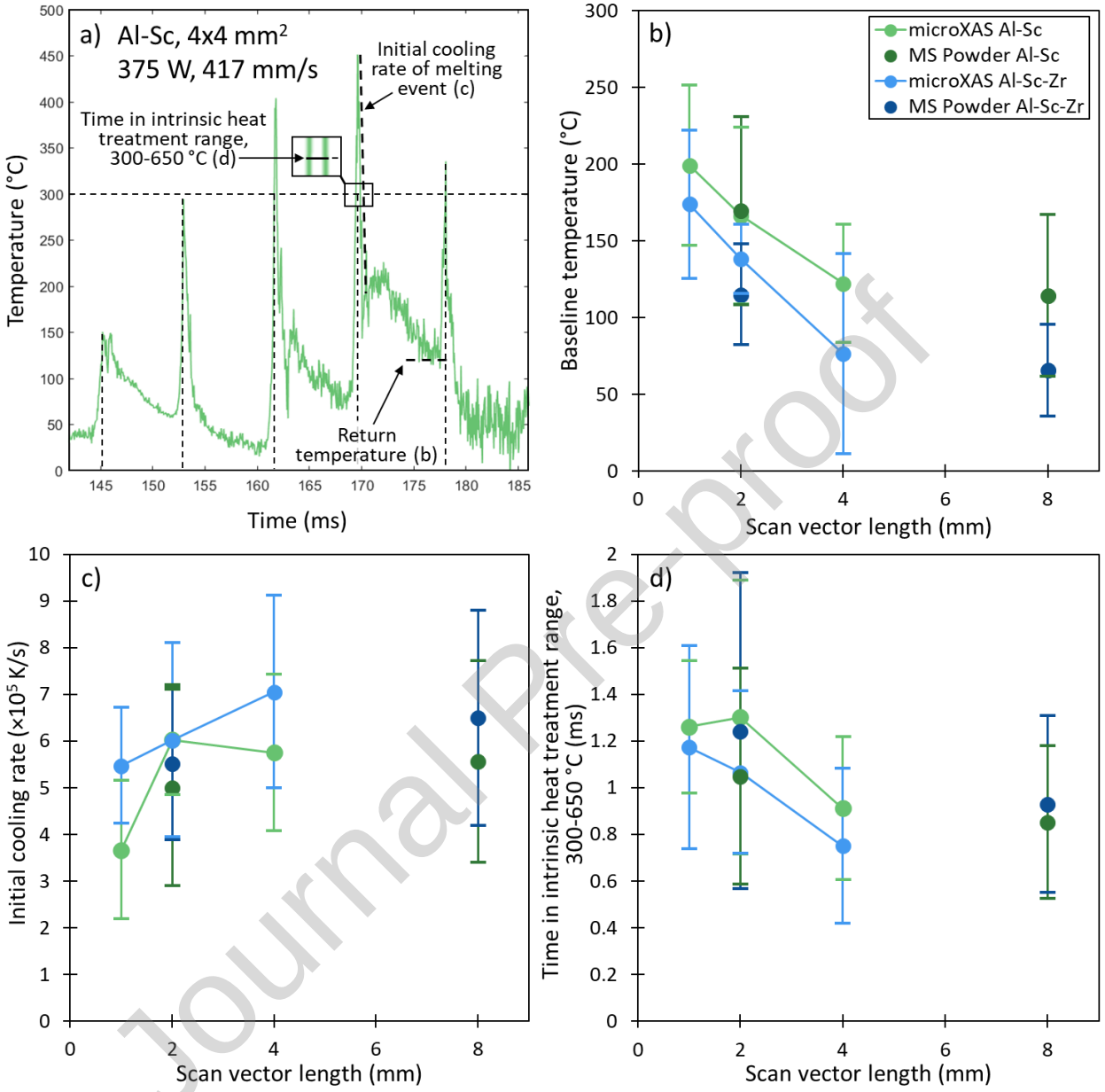

Figure 6: (a) Thermal history of diffraction volume, determined from Al(200) peak tracking before and after the melting event (at 170 ms), shown as an example for a 4×4 mm^2 Al-Sc sample processed at 375 W, 417 mm/s. **(b-d)** Summary analysis of multiple thermal histories, showing the dependence on laser scan vector length upon **(b)** the return temperature, given as the minimum temperature reached before subsequent heating; **(c)** the initial cooling rate of the melting event, given as the steepest initial linear slope of any peak; and **(d)** the time in the intrinsic heat-treatment range (between 300-650 °C), as calculated by the linear slope. The 1×1, 2×2, and 4×4 mm^2 samples produced at the microXAS beamline are shown in light color and the 8×2 mm^2 samples (alternating layers scanned at 0° and 90° rotation, with 8 mm and 2 mm scan vectors respectively) produced at the MS Powder beamline are shown in dark color. Al-Sc samples are shown in green and Al-Sc-Zr samples in blue.

3.3 Precipitation of primary $L1_2$-Al_3(Sc,Zr) on solidification

In addition to quantifying the solidification and cooling behavior in single scan fields within multilayer builds of Al-Sc(-Zr), reactions between elemental Al, Sc, and Zr powder particles were studied. Scandium and zirconium are expected to exothermically react with, and dissolve in, molten aluminum [30], nucleating randomly-oriented submicron $L1_2$-Al_3(Sc,Zr) precipitates in the melt pool upon cooling, which then nucleate α-Al matrix grains due to the similar lattice constants (0.410 nm for Al_3Sc, 0.408 nm for Al_3Zr, and 0.405 nm for α-Al) [56, 57]. *Operando* X-ray diffraction experiments captured the disappearance of Sc and Zr particles during L-PBF, as shown in **Figure 3**, and also captured the appearance of peaks corresponding to cubic $L1_2$-Al_3(Sc,Zr) precipitates, as shown in **Figure 7a**. The latter figure shows the evolution of the Al(111) and (200) peaks through laser melting in an Al-0.52Sc sample measured at the microXAS beamline, with a new peak corresponding to the $L1_2$-Al_3Sc (210) appearing after the first full melting event (as indicated by the characteristic leftward shift and reduction in peak intensity of Al(111) and (200) peaks) at 139 ms. Although the Al(111) peak disappears between 140 and 170 ms, a (200) peak located around 30.8 Å is still observed in this time interval. This peak likely corresponds to the $L1_2$(200) peak belonging to Al_3(Sc,Zr) precipitates which form rapidly in the melt, which is supported by the fact that the $L1_2$(200) peak at 30.8 Å and $L1_2$(210) peak at 34.2 Å appear at the same time (t=140 ms). As the $L1_2$-Al_3(Sc,Zr) precipitates have the same crystal structure (f.c.c.) as the α-Al matrix, the $L1_2$(200) peak overlaps the Al(200) peak and is generally indistinguishable, except if, as in this case, the α-Al matrix is in the liquid phase while the $L1_2$-Al_3(Sc,Zr) precipitates are solidified. Additionally, as the $L1_2$-Al_3(Sc,Zr) phase has a slightly larger lattice parameter (0.408-0.410 nm) compared to the α-Al matrix (0.405 nm), at room temperature the $L1_2$(200) peak is observed slightly shifted to the left of the Al(200) peak, as expected. Additional data from *operando* L-PBF experiments capturing the simultaneous disappearance of peaks corresponding to h.c.p. Sc/Zr particles and appearance of peaks corresponding to f.c.c. $L1_2$-Al_3(Sc,Zr) precipitates are given in the Supplemental Information (**Figure S6**).

Figures 7(b,c) show cross-sectional microstructures of the **(b)** Al-0.52Sc and **(c)** Al-0.26Sc-0.26Zr alloys after five layers of L-PBF, featuring the melt pool morphology and $L1_2$ precipitate size and distribution. The top surface of the samples were lightly polished for prior top-down imaging, so **Figures 6(b,c)** depict the lower layers. Nanoscale cubic $L1_2$ precipitates are observed at the base of the melt pool roughly 20-40 µm below the polished top surface of the samples. The Al_3Sc and Al_3(Sc,Zr) primary precipitates have an average diameter of 120-135 nm (n=335) and 112-125 nm (n=692) respectively. Only one solidified melt pool is observed, likely for two reasons: (i) the depth of the melt pool during laser melting is greater than 150 µm, suggesting that all five 30-µm layers are remelted even during the fifth laser pass; and (ii) the top of the melt pool was removed via polishing. Below the melt pool is the original microstructure of the 99.999% Al base plate, featuring large (hundreds of microns), elongated grains.

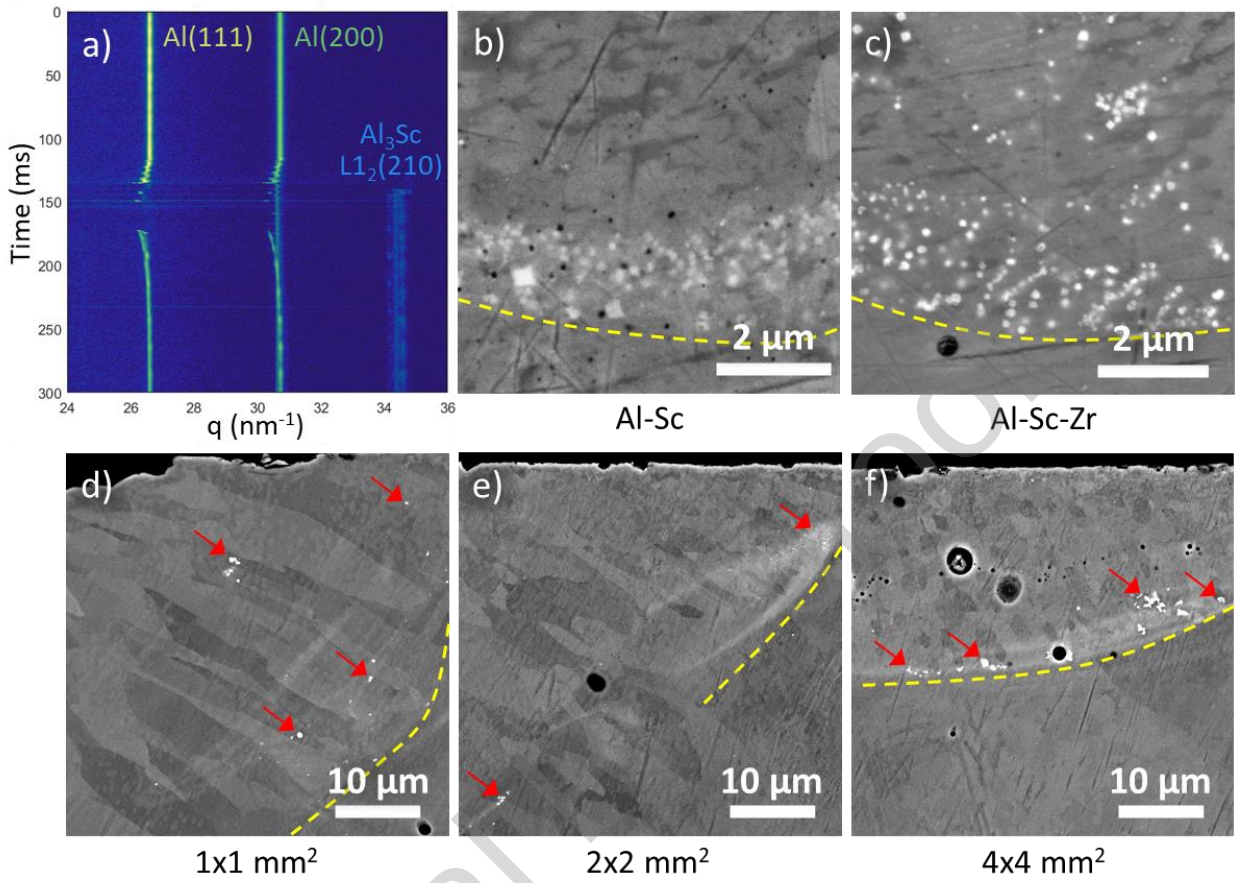

Figure 7: (a) stacked diffraction spectra for Al-0.52Sc produced at the microXAS beamline (375 W, 521 mm/s), showing the appearance of the cubic $L1_2$-Al_3Sc(210) peak at 139 ms, just after the melting event. **(b,c)** Cross-sectional views near bottom of solidified melt pool of **(b)** Al-0.52Sc and **(c)** Al-0.26Sc-0.26Zr five-layer 8×2 mm^2 samples manufactured *operando* at the MS beamline (laser scan direction in and out of the plane). A band of submicron primary $L1_2$-Al_3Sc (left) and Al_3(Sc,Zr) (right) precipitates are visible along the bottom of the solidified melt pool (marked with yellow dotted line). **(d-f)** Al-0.52Sc samples produced at the microXAS beamline with different scan areas showing Al matrix grains and $L1_2$ primary precipitates (indicated with red arrows); the laser scan direction is in and out of the plane.

Figures 7(d-f) show cross-sectional microstructures of the **(d)** 1×1 mm^2, **(e)** 2×2 mm^2, and **(f)** 4×4 mm^2 samples which were built *operando* in the microXAS beamline, illustrating the grain size and shape in each sample, as well as submicron $L1_2$-Al_3Sc precipitates present at the bottom of the melt pools. The average grain sizes (long axis) of the 1×1, 2×2, and 4×4 mm^2 samples respectively are 10.1 ± 5.1 µm (n=55), 4.7 ± 2.4 µm (n=161), and 1.9 ± 0.6 µm (n=62). As previously mentioned, this trend of increasing grain size with decreasing sample size is expected based on the increasing cooling rates (300-500, 500-600, and 600-700 K/ms for the 1×1, 2×2, and 4×4 mm^2, respectively), shown in **Figure 6b**. Assuming that each grain is nucleated by one $L1_2$-Al_3Sc precipitate (which may or may not be visible in the cross-section), the rapidly changing solidification and subsequent cooling rates observed in the larger samples (4×4 and 8×2 mm^2) generate more $L1_2$ precipitates in the melt pool, leading to a higher number of smaller, equiaxed, randomly oriented α-Al matrix grains. This is beneficial for strength, but may be

detrimental for creep resistance, due to diffusional creep. Conversely, the larger grains in the 1×1 mm^2 sample are probably nucleated by larger primary $L1_2$-Al_3Sc precipitates. The cooling rate trends in **Figure 6** and comparable cooling rates between the 4×4 and 8×2 mm^2 samples indicate that the microstructure and average grain size of the 8×2 mm^2 are likely similar to those seen in the 4×4 mm^2 sample.

This work suggests that scan areas greater than 4×4 mm^2 display comparable solidification and cooling rates, heating and cooling cycles, and intrinsic heat treatments, all of which stem from sufficient time for the sample to cool between laser passes, leading to similar microstructures. This has important design consequences for parts with small feature sizes: improvements in feature resolution in L-PBF have achieved microfeatures as small as 60 µm [58], well below the studied sample area of 1×1 mm^2 in this work. Designers must be aware of the microstructural differences of these small feature sizes, due to the thermal conductivity of the material, baseplate preheating effects or return temperature between scans, and intrinsic heat treatment which can accumulate throughout the build. Additionally, although aluminum alloys were the focus of this study, pure Al has a much higher thermal conductivity (270 W/mK) [59] compared to other popular alloys for L-PBF, such as AlSi10Mg (115-130 W/mK) [60], 316 stainless steel (16 W/mK), Inconel 625 and 718 (10 and 11 W/mK, respectively), and Ti-6Al-4V (7 W/mK). These alloys are thus likely to exhibit large differences in cooling rates, show greater microstructural differences between small and large feature sizes, and exhibit a larger feature-size "threshold" beyond which uniform microstructures can be assumed (taking 4×4 mm^2 as the example threshold feature size in this study). This threshold feature size and the microstructure differences for features below that size must be determined for each alloy individually as part of the alloy and part design process.

4 Conclusions

O*perando* selective laser melting of elemental powder blends with Al-0.52Sc and Al-0.26Sc-0.26Zr (at.%) compositions was performed on a custom miniSLM machine at the Swiss Light Source (SLS), leading to the following observations:

- High-speed synchrotron X-ray diffraction reveals that, upon laser melting, an elemental blend of Sc, Zr, and Al powders reacts to create $L1_2$-Al_3(Sc,Zr) precipitates. Reaction occurs when the Sc and Zr particles reach ~400-650 °C (well below their melting points), indicating that solid Sc/Zr reacts with molten Al, likely *via* dissolution/precipitation. This reaction takes approximately 300 µs, as captured by the diffraction patterns of the elemental Sc/Zr peaks diminishing in intensity over six 50-µs timesteps.
- Return temperatures reached between subsequent laser passes are lower in the largest (4×4 and 8×2 mm^2) samples and higher in the smallest samples (1×1 and 2×2 mm^2), due to the longer time available for the sample to cool while the laser completes its pass. Correspondingly, initial cooling rates after solidification are slowest in the smaller samples (3-5 × 10^5 K/s) and fastest in the larger samples (7-8 × 10^5 K/s), indicating a larger thermal gradient between the melt pool and surrounding material. As a result, the larger samples experience the shortest intrinsic heat treatment (defined as the time spent between 300 and 650 °C - 0.7-0.9 ms per laser pass), since the initial cooling rates are the fastest, whereas the smaller samples experience almost double that time (1.2-1.3 ms) in the intrinsic heat treatment range.
- As-solidified alloys exhibit 100-130 nm primary $L1_2$-Al_3(Sc,Zr) precipitates at the base of the melt pool with elongated columnar Al matrix grains growing in the direction of the solidification front towards the sample surface.

- The long axis of the grains decreases from 10 ± 5 µm for the 1×1 mm^2 sample to 5 ± 2 µm for the 2×2 mm^2 and 2 ± 0.6 µm for the 4×4 mm^2 samples, consistent with the decreasing trend in cooling rate. A slower cooling rate leads to larger, more elongated grains growing in the direction of the solidification front, whereas a faster cooling rate results in smaller, more equiaxed grains.

This work shows that elemental blends can be successfully used to create $L1_2$-Al_3(Sc,Zr) primary precipitates which act as grain refiners in an Al-Sc(-Zr) alloy, even at a very low ratio of Sc/Al and Zr/Al particles (~1:130). *Operando* X-ray diffraction showing the evolution of the Al, Sc, and Zr particles indicates that the reaction between Al and the Sc/Zr particles occurs at temperatures near the melting point of Al (~650 °C), so that melting of the Sc/Zr particles (at 1541 and 1855 °C) is not necessary, consistent with the exothermic nature of the reaction.

The feature size has a major influence on the part's local thermal history. As the 4×4 and 8×2 mm^2 samples exhibit comparable return temperatures, initial cooling rates, and intrinsic heat treatment times, it can be assumed that the 8×2 mm^2 has a comparable microstructure with respect to primary precipitate size and number density, and grain size. From this, 4×4 mm^2 is taken as the feature threshold size above which microstructure differences are negligible.

The difference in return temperature, initial solidification and cooling rate, intrinsic heat treatment, and resulting microstructure must all be considered when designing parts with small feature sizes. Features below a certain threshold size - where the time between laser passes is sufficiently long that microstructures differences are negligible - will result in different primary precipitate sizes and number densities, grain sizes, and potentially secondary precipitation effects due to the cumulative intrinsic heat treatment during layer-wise building. These effects can be mitigated by keeping features above this threshold size or by changing the laser parameters to account for different cooling rates and preheating effects.

5 Acknowledgements

This research received funding from the US Army Research Laboratory (award W911NF-19-2-0092). JAG was supported by the Army Research Laboratory (ARL) Oak Ridge Associated Universities (ORAU) via a Journeyman Fellowship grant, and she thanks Dr. Jon-Erik Mogonye (ARL) for numerous useful discussions. JAG also thanks the Embassy of Switzerland in the U.S. for granting a ThinkSwiss Research Scholarship, allowing travel to Switzerland for research purposes. The authors acknowledge the Paul Scherrer Institut (Villigen, Switzerland) for provision of synchrotron radiation beamtime at beamlines MS and MicroXAS of the SLS. This work made use of the EPIC facility of Northwestern University's NU*ANCE* Center, which has received support from the Soft and Hybrid Nanotechnology Experimental (SHyNE) Resource (NSF ECCS-1542205); the MRSEC program (NSF DMR-1720139) at the Materials Research Center; the International Institute for Nanotechnology (IIN); the Keck Foundation; and the State of Illinois, through the IIN. This work also made use of the Materials Characterization and Imaging Facility which receives support from the MRSEC Program (NSF DMR-1720139) of the Materials Research Center at Northwestern University. This work was further supported by (1) the PREcision Additive Manufacturing of Precious metals Alloys (PREAMPA) project, funded by the ETH board and the Swiss watch and precious metals industry; (2) the Additive Manufacturing and Metallic Microstructures (AM3) project, funded by the Competence Center for Materials Science and Technology (CCMX) and the Swiss watch and precious metals industry.

6 References

[1] L. Hitzler, M. Merkel, W. Hall, A. Öchsner, A Review of Metal Fabricated with Laser- and Powder-Bed Based Additive Manufacturing Techniques: Process, Nomenclature, Materials, Achievable Properties, and its Utilization in the Medical Sector, Advanced Engineering Materials 20(5) (2018).
[2] J.H. Martin, B.D. Yahata, J.M. Hundley, J.A. Mayer, T.A. Schaedler, T.M. Pollock, 3D printing of high-strength aluminium alloys, Nature 549(7672) (2017) 365-369.
[3] I. Kunce, M. Polanski, J. Bystrzycki, Structure and hydrogen storage properties of a high entropy ZrTiVCrFeNi alloy synthesized using Laser Engineered Net Shaping (LENS), International Journal of Hydrogen Energy 38(27) (2013) 12180-12189.
[4] H. Dobbelstein, E.L. Gurevich, E.P. George, A. Ostendorf, G. Laplanche, Laser metal deposition of a refractory TiZrNbHfTa high-entropy alloy, Additive Manufacturing 24 (2018) 386-390.
[5] H. Dobbelstein, M. Thiele, E.L. Gurevich, E.P. George, A. Ostendorf, Direct Metal Deposition of Refractory High Entropy Alloy MoNbTaW, Physics Procedia 83 (2016) 624-633.
[6] X. Chen, L. Yan, S. Karnati, Y. Zhang, F. Liou, Fabrication and Characterization of AlxCoFeNiCu1−x High Entropy Alloys by Laser Metal Deposition, Coatings 7(4) (2017).
[7] S. Ewald, F. Kies, S. Hermsen, M. Voshage, C. Haase, J.H. Schleifenbaum, Rapid Alloy Development of Extremely High-Alloyed Metals Using Powder Blends in Laser Powder Bed Fusion, Materials (Basel) 12(10) (2019).
[8] C. Haase, F. Tang, M.B. Wilms, A. Weisheit, B. Hallstedt, Combining thermodynamic modeling and 3D printing of elemental powder blends for high-throughput investigation of high-entropy alloys – Towards rapid alloy screening and design, Materials Science and Engineering: A 688 (2017) 180-189.
[9] D. Lin, L. Xu, X. Li, H. Jing, G. Qin, H. Pang, F. Minami, A Si-containing FeCoCrNi high-entropy alloy with high strength and ductility synthesized in situ via selective laser melting, Additive Manufacturing (2020).
[10] M.A. Melia, S.R. Whetten, R. Puckett, M. Jones, M.J. Heiden, N. Argibay, A.B. Kustas, High-throughput additive manufacturing and characterization of refractory high entropy alloys, Applied Materials Today 19 (2020).
[11] M. Moorehead, K. Bertsch, M. Niezgoda, C. Parkin, M. Elbakhshwan, K. Sridharan, C. Zhang, D. Thoma, A. Couet, High-throughput synthesis of Mo-Nb-Ta-W high-entropy alloys via additive manufacturing, Materials & Design 187 (2020).
[12] A. Grigoriev, I. Polozov, V. Sufiiarov, A. Popovich, In-situ synthesis of Ti2AlNb-based intermetallic alloy by selective laser melting, Journal of Alloys and Compounds 704 (2017) 434-442.
[13] I. Polozov, V. Sufiiarov, A. Popovich, D. Masaylo, A. Grigoriev, Synthesis of Ti-5Al, Ti-6Al-7Nb, and Ti-22Al-25Nb alloys from elemental powders using powder-bed fusion additive manufacturing, Journal of Alloys and Compounds 763 (2018) 436-445.
[14] B. Zhang, J. Chen, C. Coddet, Microstructure and Transformation Behavior of in-situ Shape Memory Alloys by Selective Laser Melting Ti–Ni Mixed Powder, Journal of Materials Science & Technology 29(9) (2013) 863-867.
[15] K. Zhuravleva, M. Bonisch, K.G. Prashanth, U. Hempel, A. Helth, T. Gemming, M. Calin, S. Scudino, L. Schultz, J. Eckert, A. Gebert, Production of Porous beta-Type Ti-40Nb Alloy for Biomedical Applications: Comparison of Selective Laser Melting and Hot Pressing, Materials (Basel) 6(12) (2013) 5700-5712.
[16] M. Fischer, D. Joguet, G. Robin, L. Peltier, P. Laheurte, In situ elaboration of a binary Ti-26Nb alloy by selective laser melting of elemental titanium and niobium mixed powders, Mater Sci Eng C Mater Biol Appl 62 (2016) 852-9.
[17] S.L. Sing, W.Y. Yeong, F.E. Wiria, Selective laser melting of titanium alloy with 50 wt% tantalum: Microstructure and mechanical properties, Journal of Alloys and Compounds 660 (2016) 461-470.

[18] L. Yan, Y. Yuan, L. Ouyang, H. Li, A. Mirzasadeghi, L. Li, Improved mechanical properties of the new Ti-15Ta-xZr alloys fabricated by selective laser melting for biomedical application, Journal of Alloys and Compounds 688 (2016) 156-162.
[19] T. Nagase, T. Hori, M. Todai, S.-H. Sun, T. Nakano, Additive manufacturing of dense components in beta-titanium alloys with crystallographic texture from a mixture of pure metallic element powders, Materials & Design 173 (2019).
[20] C. Wang, X.P. Tan, Z. Du, S. Chandra, Z. Sun, C.W.J. Lim, S.B. Tor, C.S. Lim, C.H. Wong, Additive manufacturing of NiTi shape memory alloys using pre-mixed powders, Journal of Materials Processing Technology 271 (2019) 152-161.
[21] J.C. Wang, Y.J. Liu, P. Qin, S.X. Liang, T.B. Sercombe, L.C. Zhang, Selective laser melting of Ti–35Nb composite from elemental powder mixture: Microstructure, mechanical behavior and corrosion behavior, Materials Science and Engineering: A 760 (2019) 214-224.
[22] N. Kang, X. Lin, C. Coddet, X. Wen, W. Huang, Selective laser melting of low modulus Ti-Mo alloy: α/β heterogeneous conchoidal structure, Materials Letters 267 (2020).
[23] R. Zhao, J. Gao, H. Liao, N. Fenineche, C. Coddet, Selective laser melting of elemental powder blends for fabrication of homogeneous bulk material of near-eutectic Ni–Sn composition, Additive Manufacturing (2020).
[24] Y. Guo, M.-C. Zhao, B. Xie, Y.-C. Zhao, D. Yin, C. Gao, C. Shuai, A. Atrens, In Vitro Corrosion Resistance and Antibacterial Performance of Novel Fe–xCu Biomedical Alloys Prepared by Selective Laser Melting, Advanced Engineering Materials (2021).
[25] P. Wang, L. Deng, K.G. Prashanth, S. Pauly, J. Eckert, S. Scudino, Microstructure and mechanical properties of Al-Cu alloys fabricated by selective laser melting of powder mixtures, Journal of Alloys and Compounds 735 (2018) 2263-2266.
[26] R. Martinez, I. Todd, K. Mumtaz, In situ alloying of elemental Al-Cu12 feedstock using selective laser melting, Virtual and Physical Prototyping 14(3) (2019) 242-252.
[27] E.O. Olakanmi, Selective laser sintering/melting (SLS/SLM) of pure Al, Al–Mg, and Al–Si powders: Effect of processing conditions and powder properties, Journal of Materials Processing Technology 213(8) (2013) 1387-1405.
[28] P. Vora, K. Mumtaz, I. Todd, N. Hopkinson, AlSi12 in-situ alloy formation and residual stress reduction using anchorless selective laser melting, Additive Manufacturing 7 (2015) 12-19.
[29] N. Kang, P. Coddet, H. Liao, C. Coddet, Macrosegregation mechanism of primary silicon phase in selective laser melting hypereutectic Al – High Si alloy, Journal of Alloys and Compounds 662 (2016) 259-262.
[30] J.A. Glerum, C. Kenel, T. Sun, D.C. Dunand, Synthesis of precipitation-strengthened Al-Sc, Al-Zr and Al-Sc-Zr alloys via selective laser melting of elemental powder blends, Additive Manufacturing 36 (2020).
[31] R.W. Cunningham, C. Zhou, T. Sun, K. Fezzaa, N. Parab, Keyhole threshold and morphology in laser melting revealed by ultrahighspeed xray imaging, Science (2019).
[32] C. Zhao, K. Fezzaa, R.W. Cunningham, H. Wen, F. De Carlo, L. Chen, A.D. Rollett, T. Sun, Real-time monitoring of laser powder bed fusion process using high-speed X-ray imaging and diffraction, Sci Rep 7(1) (2017) 3602.
[33] C. Kenel, D. Grolimund, J.L. Fife, V.A. Samson, S. Van Petegem, H. Van Swygenhoven, C. Leinenbach, Combined in situ synchrotron micro X-ray diffraction and high-speed imaging on rapidly heated and solidified Ti–48Al under additive manufacturing conditions, Scripta Materialia 114 (2016) 117-120.
[34] C. Kenel, D. Grolimund, X. Li, E. Panepucci, V.A. Samson, D.F. Sanchez, F. Marone, C. Leinenbach, In situ investigation of phase transformations in Ti-6Al-4V under additive manufacturing conditions combining laser melting and high-speed micro-X-ray diffraction, Sci Rep 7(1) (2017) 16358.

[35] Y. Chen, S.J. Clark, C.L.A. Leung, L. Sinclair, S. Marussi, M.P. Olbinado, E. Boller, A. Rack, I. Todd, P.D. Lee, In-situ Synchrotron imaging of keyhole mode multi-layer laser powder bed fusion additive manufacturing, Applied Materials Today 20 (2020).
[36] J.-B. Forien, N.P. Calta, P.J. DePond, G.M. Guss, T.T. Roehling, M.J. Matthews, Detecting keyhole pore defects and monitoring process signatures during laser powder bed fusion: a correlation between in situ pyrometry and ex situ X-ray radiography, Additive Manufacturing (2020).
[37] Q. Guo, C. Zhao, M. Qu, L. Xiong, S.M.H. Hojjatzadeh, L.I. Escano, N.D. Parab, K. Fezzaa, T. Sun, L. Chen, In-situ full-field mapping of melt flow dynamics in laser metal additive manufacturing, Additive Manufacturing 31 (2020).
[38] S.M.H. Hojjatzadeh, N.D. Parab, Q. Guo, M. Qu, L. Xiong, C. Zhao, L.I. Escano, K. Fezzaa, W. Everhart, T. Sun, L. Chen, Direct observation of pore formation mechanisms during LPBF additive manufacturing process and high energy density laser welding, International Journal of Machine Tools and Manufacture 153 (2020).
[39] A.A. Martin, N.P. Calta, S.A. Khairallah, J. Wang, P.J. Depond, A.Y. Fong, V. Thampy, G.M. Guss, A.M. Kiss, K.H. Stone, C.J. Tassone, J. Nelson Weker, M.F. Toney, T. van Buuren, M.J. Matthews, Dynamics of pore formation during laser powder bed fusion additive manufacturing, Nature Communications 10(1) (2019).
[40] C.L.A. Leung, X-ray imaging of powder consolidation during laser additive manufacturing, School of Materials, University of Manchester, 2017.
[41] C.L.A. Leung, S. Marussi, R.C. Atwood, M. Towrie, P.J. Withers, P.D. Lee, In situ X-ray imaging of defect and molten pool dynamics in laser additive manufacturing, Nat Commun 9(1) (2018) 1355.
[42] N.H. Paulson, B. Gould, S.J. Wolff, M. Stan, A. Greco, Correlations between thermal history and keyhole porosity in laser powder bed fusion, Additive Manufacturing (2020).
[43] S. Hocine, S. Van Petegem, U. Frommherz, G. Tinti, N. Casati, D. Grolimund, H. Van Swygenhoven, A miniaturized selective laser melting device for operando X-ray diffraction studies, Additive Manufacturing 34 (2020).
[44] S. Hocine, H. Van Swygenhoven, S. Van Petegem, C.S.T. Chang, T. Maimaitiyili, G. Tinti, D. Ferreira Sanchez, D. Grolimund, N. Casati, Operando X-ray diffraction during laser 3D printing, Materials Today 34 (2020) 30-40.
[45] J. Jiang, Y. Ma, Path Planning Strategies to Optimize Accuracy, Quality, Build Time and Material Use in Additive Manufacturing: A Review, Micromachines (Basel) 11(7) (2020).
[46] F. Herzog, Process for manufacturing a shaped article, in particular powder stereolithographic or sintering process, 2004.
[47] Y. Lu, S. Wu, Y. Gan, T. Huang, C. Yang, L. Junjie, J. Lin, Study on the microstructure, mechanical property and residual stress of SLM Inconel-718 alloy manufactured by differing island scanning strategy, Optics & Laser Technology 75 (2015) 197-206.
[48] G. Tinti, A. Bergamaschi, S. Cartier, R. Dinapoli, D. Greiffenberg, I. Johnson, J.H. Jungmann-Smith, D. Mezza, A. Mozzanica, B. Schmitt, X. Shi, Performance of the EIGER single photon counting detector, Journal of Instrumentation 10(03) (2015) C03011-C03011.
[49] Bubble: fast powder integration - pyFAI on steroids -- SNBL Software Guide 0.1 documentation, (n.d.). https://soft.snbl.eu/bubble.html. (Accessed December 14, 2020.
[50] Fast Azimuthal Integration using Python - pyFAI 0.18.0a0 documentation, (n.d.). https://pyfai.readthedocs.io/en/master/. (Accessed December 14, 2020.
[51] G.B. Skinner, H.L. Johnston, Thermal Expansion of Zirconium between 298°K and 1600°K, The Journal of Chemical Physics 21(8) (1953) 1383-1384.
[52] F.H. Spedding, J.J. Hanak, A.H. Daane, High temperature allotropy and thermal expansion of the rare-earth metals, Journal of the Less Common Metals 3(2) (1961) 110-124.

[53] B. Vrancken, Study of residual stresses in selective laser melting, Engineering Science, KU Leuven, 2016.
[54] D. Rosenthal, Mathematical Theory of Heat Distribution during Welding and Cutting, Welding Journal 20 (1941) 220-234.
[55] S. Hocine, H. Van Swygenhoven, S. Van Petegem, Verification of selective laser melting heat source models with operando X-ray diffraction data, Additive Manufacturing (2020).
[56] E. Nes, Precipitation of the metastable cubic Al3Zr-phase in subperitectic Al-Zr alloys, Acta Metall Mater 20 (1972) 499-506.
[57] Y. Harada, D.C. Dunand, Microstructure of Al3Sc with ternary transition-metal additions, Materials Science and Engineering A (2002).
[58] B. Nagarajan, Z. Hu, X. Song, W. Zhai, J. Wei, Development of Micro Selective Laser Melting: The State of the Art and Future Perspectives, Engineering 5(4) (2019) 702-720.
[59] R. Brandt, G. Neuer, Electrical Resistivity and Thermal Conductivity of Pure Aluminum and Aluminum Alloys up to and above the Melting Temperature, International Journal of Thermophysics 28(5) (2007) 1429-1446.
[60] R.R.J. Sélo, S. Catchpole-Smith, I. Maskery, I. Ashcroft, C. Tuck, On the thermal conductivity of AlSi10Mg and lattice structures made by laser powder bed fusion, Additive Manufacturing 34 (2020).
[61] Y.S. Touloukian, R.K. Kirby, R.E. Taylor, P.B. Desai, Thermal Expansion Metallic Elements and Alloys, in: C.P. University (Ed.) Defense Logistics Agency, Alexandria, VA 22314, 1975, p. 1442.

Declaration of competing interest

☐ The authors declare that they have no known competing financial interests or personal relationships that could have appeared to influence the work reported in this paper.

☒The authors declare the following financial interests/personal relationships which may be considered as potential competing interests: DCD discloses financial interests relative to Braidy Industries, which could potentially benefit from the outcomes of this research but did not influence its conduct, description, or interpretation.